Volume 2
Number 14
21 July 2021
Pages 4435–4884

Materials Advances

rsc.li/materials-advances

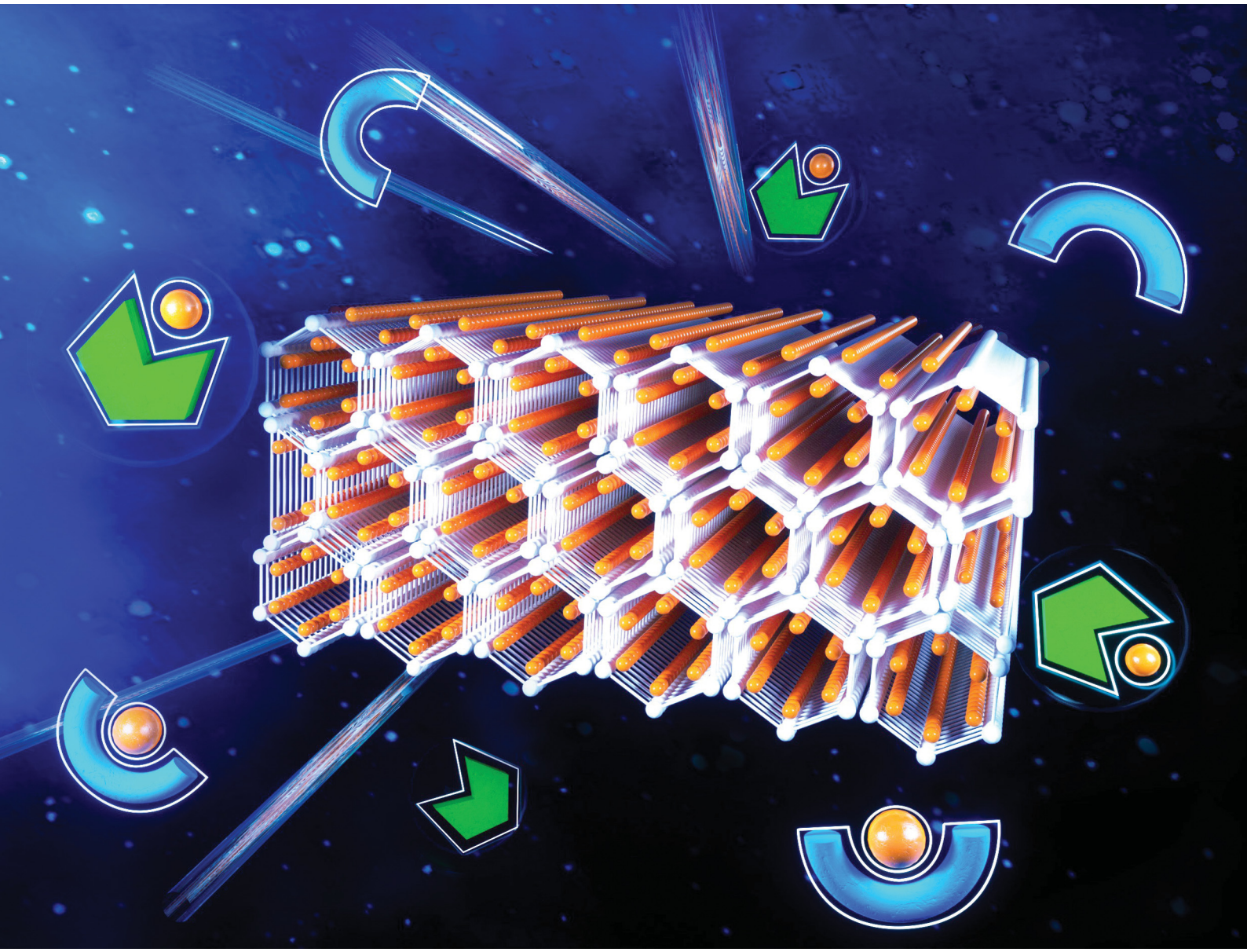

ISSN 2633-5409

ROYAL SOCIETY OF CHEMISTRY

PAPER

Shiao-Wei Kuo *et al.*

A water-soluble copper-immobilized covalent organic framework functioning as an "OFF–ON" fluorescent sensor for amino acids

Materials Advances

ROYAL SOCIETY OF CHEMISTRY

PAPER

View Article Online
View Journal | View Issue

Cite this: *Mater. Adv.*, 2021, 2, 4617

A water-soluble copper-immobilized covalent organic framework functioning as an "OFF–ON" fluorescent sensor for amino acids†

Lamiaa Reda Ahmed,[a] Ahmed F. M. EL-Mahdy,[b] Cheng-Tang Pan[ac] and Shiao-Wei Kuo *[bd]

In this paper, we describe the construction of a new fluorescent hydroxyl- and hydrazone-based covalent organic framework (**TFPB–DHTH** COF) through the one-pot polycondensation of 1,3,5-tris(4-formylphenyl)benzene (**TFPB**) and 2,5-dihydroxyterephthalohydrazide (**DHTH**) under solvothermal conditions. The synthesized **TFPB–DHTH** COF possessed high crystallinity, a regular pore structure, excellent chemical stability, and sites featuring functional groups suitable for interactions with metal ions. In addition, the **TFPB–DHTH** COF was highly soluble in water and buffer and displayed a strong fluorescence emission under UV irradiation. The fluorescence of the **TFPB–DHTH** COF was quenched selectively by Cu^{2+} ions, forming a non-fluorescent copper-immobilized **TFPB–DHTH** COF (Cu@**TFPB–DHTH** COF); the off fluorescent state of the Cu@**TFPB–DHTH** COF was efficiently and selectively switched on upon the addition of cysteine (Cys) and L-histidine (L-His). Therefore, the Cu@**TFPB–DHTH** COF functioned as an "OFF–ON" fluorescent sensor for the detection of Cys and L-His. When incorporating *N*-ethylmaleimide and Ni^{2+} ions, we could separately and selectively detect Cys and L-His, respectively. Our new sensing assay could be completed within 30 min; it provided linear relationships with respect to concentrations of Cys and L-His of 2–100 and 2–200 μM, respectively, with limits of detection of 340 and 520 nM, respectively. Our strategy highlights the possibility of using water-soluble COFs as novel fluorescent sensors for amino acids, with promise for applications industrially or in environmental remediation.

Received 17th March 2021,
Accepted 9th May 2021

DOI: 10.1039/d1ma00234a

rsc.li/materials-advances

Introduction

Cysteine (Cys) is an essential small thiol-functionalized amino acid for living cells, where it plays crucial roles in various pathological and physiological processes (*e.g.*, redox-balance regulation, anti-aging, metabolism, biocatalysis, protein synthesis, and detoxification), while also being associated with many diseases involving cancers. Cys is a significant structural and functional component of many enzymes and proteins.[1–5] Nevertheless, abnormal levels of Cys in the human body can place human health at risk. For example, a high level of Cys can be a vital factor for amyotrophic lateral sclerosis and Parkinson's, Alzheimer's, and cardiovascular diseases.[6,7] In addition, a lack of Cys can lead to symptoms such as liver damage, hair discoloration, developmental delay, and hematopoietic dysfunction.[8] Therefore, it is important to develop a simple selective, sensitive and reliable method for the detection of Cys. L-Histidine (L-His) is a natural amino acid featuring an aromatic imidazole unit; it is mainly present in the active-catalytic sites of various enzymes. L-His plays important roles in decreasing the risk of internal microtrauma bleeding and in monitoring the metal transport processes of essential biological bases.[9,10] Chronic L-His deficiency is associated significantly with Friedreich's ataxia, epilepsy, Parkinson's disease, and the inability to develop normal erythropoiesis; the overexpression of L-His in biological fluids (serum and urine) can cause hereditary metabolic disorder.[11–14] Therefore, reliable and highly sensitive detection and quantification of L-His is thus of considerable significance for therapeutic systems including clinical treatment and medicinal science.

Several analytic techniques have been reported previously for the quantitative detection of Cys and L-His, including those based on UV-Vis absorption spectroscopy, electrochemical

[a] *Institute of Medical Science and Technology, National Sun Yat-Sen University, Kaohsiung 80424, Taiwan*
[b] *Department of Materials and Optoelectronic Science, National Sun Yat-Sen University, Kaohsiung, 80424, Taiwan. E-mail: kuosw@faculty.nsysu.edu.tw*
[c] *Department of Mechanical and Electro-Mechanical Engineering, National Sun Yat-Sen University, Kaohsiung 80424, Taiwan*
[d] *Department of Medicinal and Applied Chemistry, Kaohsiung Medical University, Kaohsiung 807, Taiwan*

† Electronic supplementary information (ESI) available. See DOI: 10.1039/d1ma00234a

analysis, capillary electrophoresis, spectrofluorimetry, immunoassaying, and high-performance liquid chromatography (HPLC).[15–21] These techniques, however, have various shortcomings: they can be time-consuming and/or operationally inconvenient, and they can require cumbersome and/or expensive instruments. Recently, photophysical analytical techniques, particularly fluorescence-based versions, have become widespread for their high sensitivity, low detection limits, low cost, convenience, and suitability for bioimaging.[22–30] The design of novel fluorescent probes including fluorophoric molecules, metal nanoclusters, and carbon dots (CDs), has also gained recognition.[31,32] The detection mechanisms of these fluorescent probes have depended mainly on interactions between the functional groups of the probes and the thiol/amino groups of Cys or the imidazole/amino groups of L-His. In addition, mechanisms involving the coordination displacement of ligand–metal probes by Cys and L-His have also been reported. For example, Park *et al.* described the label-free detection of Cys through the fluorescence turn-on of metallophilic Hg–Au nanoclusters upon coordination of its Hg^{2+} moieties with Cys through its thiol group.[23] Moreover, Yan *et al.* demonstrated water-soluble CDs as a novel fluorescent probe for the detection of Cys through the turn-on fluorescence of a CD–Hg^{2+} complex after Hg^{2+}–Cys coordination.[24] Das *et al.* developed a ligand-displacement approach for the detection of L-His by using a fluorescent $[Cu(LH_2)Cl_2]\cdot 2H_2O$ probe (where LH_2 is a pyridoxal-semicarbazide Schiff base) as a naked-eye fluorescent sensor.[33] These few examples suggest that there remains much room for the development of rapidly indicating, easy-to-prepare, versatile and inexpensive fluorescent probes for the detection of Cys and L-His.

Covalent organic frameworks (COFs) are drawing interest as innovative porous crystalline polymers, formed from assembling organic building units into ordered structures through strong covalent bonds.[34–37] Similar to conventional crystalline porous materials [*e.g.*, zeolites and metal organic frameworks (MOFs)], COFs possess precise predesigned structures and tailorable functionality, thereby allowing structural and chemical control over their particular functions.[37–39] In addition to overcoming the shortcomings of the weakly crystalline structures and irregular pore distributions of most inorganic porous materials, COFs can also operate without the potential for collapse that often occurs for MOFs in organic solvents and water.[40] Moreover, COFs can display high thermal and chemical stabilities, low densities, extremely high surface areas, regular porosity, excellent crystalline forms, and tunable structures and pore sizes.[41–44] Accordingly, COFs are promising candidate materials for various applications, including the removal of pollutants from wastewater, (photo)catalysis, energy storage, gas separation and uptake, sensing, solar cells, the detection and removal of toxic metal ions, and photodynamic therapy.[45–55]

Various COFs displaying fluorescence characteristics have been constructed previously and applied as chemosensors for pH, electron-rich arenes, mercury ions, 2,4,6-trinitrophenol, and anions.[56–63] For biosensing applications, COF materials can have several attractive features, including high conductivity, high loading capacity, and biocompatibility. First, the uniform and crystalline structures of COFs can accelerate the migration of charged particles and, thereby, enhance their biosensor response rates.[64] Second, the regular porosity of COFs can cause them to have large specific active surface areas and high surface free energies, leading to very high loading capacities when combined with organic molecules.[65] Third, the biocompatibility of COF materials can provide appropriate microenvironments for biomolecules, thereby maintaining their activity. Together, these features appear to make COFs more designable than conventional porous materials based on organic polymers and inorganic materials.[66,67]

The distinctive photophysical and chemical properties of COFs encouraged us to develop one for the detection of L-His and L-Cys. Biosensors based on COFs remain rare and, to the best of our knowledge, the use of water-soluble COFs for the detection of amino acids has not been reported previously. In this paper, we describe the preparation of a water-soluble copper-immobilized COF (Cu@**TFPB–DHTH** COF) through the polycondensation of 1,3,5-tris(4-formylphenyl)benzene (**TFPB–3CHO**) and 2,5-dihydroxyterephthalohydrazide (**DHTH**) under solvothermal conditions (forming the **TFPB–DHTH** COF) and subsequent incorporation of Cu^{2+} ions (Scheme 1). The **TFPB–DHTH** COF displayed high chemical stability and a strong fluorescence emission, while the Cu@**TFPB–DHTH** COF exhibited a non-fluorescent emission. Interestingly, the addition of Cys or L-His to the fluorescence-off state of the Cu@**TFPB–DHTH** COF stimulated the snatching and seizure of the Cu^{2+} ions and, thereby, switched on the fluorescence emission of the **TFPB–DHTH** COF (Scheme 2). Therefore, we also studied the use of the Cu@**TFPB–DHTH** COF as a water-soluble "OFF–ON" fluorescent sensor for the detection of Cys and L-His.

Experimental section

Materials

Tetrakis(triphenylphosphine)palladium(0), 2,5-dihydroxy-1,4-benzenedicarboxylic acid, and 1,3,5-tribromobenzene were purchased from Acros. 4-Formylphenylboronic acid, Cys, L-His, and 10× PBS buffer were obtained from Sigma-Aldrich. Potassium carbonate, mesitylene, and hydrazine hydrate (98%) were purchased from Alfa Aesar. Methanol (MeOH), ethanol (EtOH), tetrahydrofuran (THF), 1,4-dioxane, glacial acetic acid, acetone, and dichloromethane (DCM) were obtained in analytical grade and were used without purification.

Measurements

Transmission electron microscopy (TEM) was performed using a JEOL-2100 scanning electron microscope, operated at an accelerating voltage of 200 kV. Field-emission scanning electron microscopy (FE-SEM) was conducted using a JEOL JSM-7610F scanning electron microscope; the COF sample was subjected to Pt sputtering for 100 s prior to observation. The **TFPB–DHTH** COF sample for UV-Vis adsorption spectroscopy was dissolved in

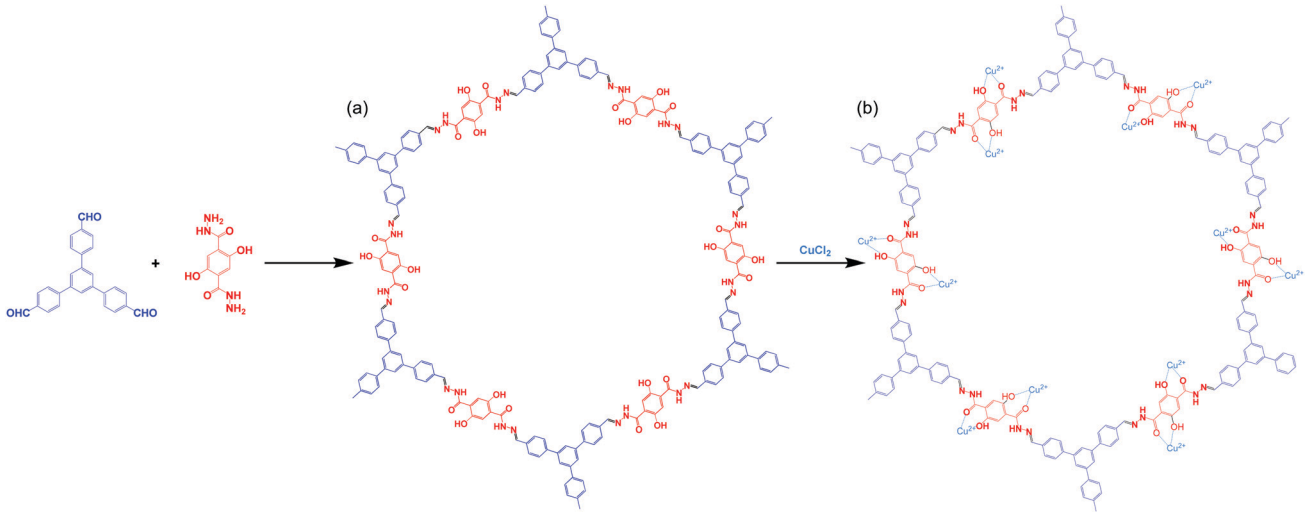

Scheme 1 Synthesis of the **TFPB–DHTH** COF and the Cu@**TFPB–DHTH** COF.

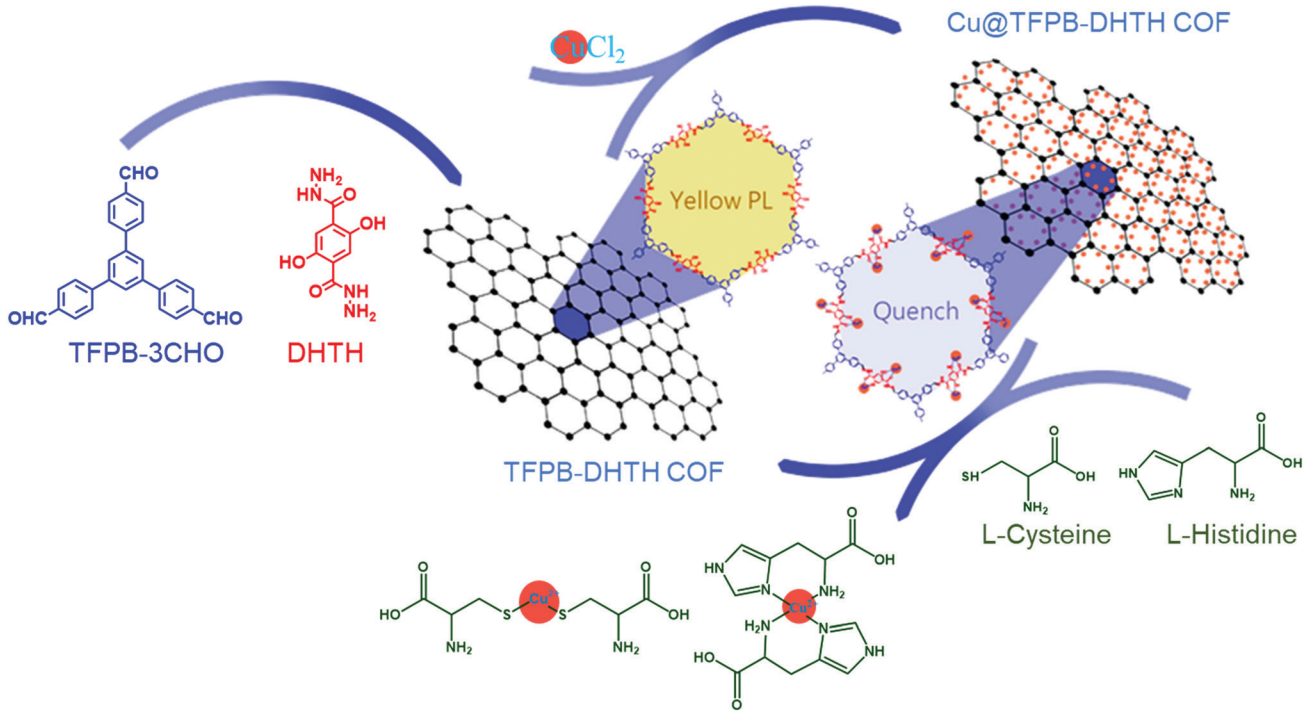

Scheme 2 Schematic representation of the fluorescence sensing of Cys and L-His using the Cu@**TFPB–DHTH** COF.

water and transferred to a small quartz cell ($0.2 \times 1.0 \times 4.5$ cm^3); the spectrum was recorded using a JASCO V-770 UV-visible-NIR spectrophotometer. Fluorescence emission spectra were recorded using a LabGuide X350 spectrometer; samples were placed in a quartz cuvette having a path length of 1 cm and a slit width of 10×10 nm. The photoluminescence quantum yield (PLQY) of the **TFPB–DHTH** COF was recorded using a HORIBA Fluorolog-3 photon counting spectrofluorometer system equipped with a Quanta-φ 6-inch integrating sphere. All pH measurements were performed using a SUNTEX SP-2100 pH meter.

Synthesis of 2,5-dihydroxyterephthalohydrazide (DHTH). A 100 mL two-neck round-bottom flask was charged with 2,5-dihydroxy-1,4-benzenedicarboxylic acid diethyl ester[68] (2.00 g, 7.86 mmol), EtOH (80 mL), and hydrazine hydrate (10 mL). The mixture was heated under reflux at 90 °C for 20 h, forming a large amount of a pale-yellow precipitate. The solid was filtered off under vacuum and washed several times with EtOH. **DHTH** (1.5 g, 85%) was obtained after two recrystallizations of the crude solid from EtOH (Scheme S1, ESI†). FTIR: 3397, 3307, 3044, 1630, 1541, 1505, 1349, 1255, 1161, 955 cm^{-1} (Fig. S1, ESI†). ^{1}H NMR (500 MHz, DMSO-d_6) δ (ppm): 11.57

(s, 2OH, 2H), 10.01 (s, 2NH, 2H), 7.33 (s, 2CH, 2H), 4.67 (s, $2NH_2$, 4H) (Fig. S2). ^{13}C NMR (100 MHz, DMSO-d_6) δ (ppm): 167.37, 151.50, 119.73, 115.59 (Fig. S3, ESI†).

Synthesis of 1,3,5-Tris(4-formylphenyl)benzene (TFPB–3CHO). A 100 mL two-neck round-bottom flask was charged with 1,3,5-tribromobenzene (1.00 g, 3.18 mmol), tetrakis(triphenylphosphine) palladium(0) (184 mg, 0.160 mmol), potassium carbonate (2.64 g, 19.1 mmol), and 4-formylphenylboronic acid (2.86 g, 19.1 mmol). The mixed solids were evacuated under pressure for 30 min and then a mixture of 1,4-dioxane (40 mL) and water (7.5 mL) was added slowly under a stream of N_2. The resulting mixture was heated at 110 °C for 40 h, and then cooled to room temperature over 1 h. The mixture was poured into ice-water (200 mL), producing a white precipitate. After vacuum filtration, the crude solid was washed several times with water and MeOH (Scheme S2, ESI†). The crude solid was purified through a short chromatographic column (SiO_2; EtOAc/*n*-hexane, 1 : 9) to yield **TFPB–3CHO** as a white solid (990 mg, 80%). FTIR: 3040, 2811, 2717, 1685, 1604, 1563, 1420, 1380, 1214, 1170 cm^{-1} (Fig. S4, ESI†). ^{1}H NMR (500 MHz, DMSO-d_6) δ (ppm): 10.08 (s, 3CHO, 3H), 8.18 (d, J = 8.8 Hz, 6H), 8.16 (s, 3H), 8.05 (d, J = 8.8 Hz, 6H) (Fig. S5, ESI†). ^{13}C NMR (100 MHz, DMSO-d_6) δ (ppm): 194.14, 146.07, 141.39, 136.08, 130.80, 128.53, 126.86 (Fig. S6, ESI†).

Synthesis of TFPB–DHTH COF. In a 25 mL tube, **TFPB–3CHO** (100 mg, 0.256 mmol, 1 eq.) and **DHTH** (86.9 mg, 0.384 mmol, 1.5 eq.) were suspended in a mixture of 1,4-dioxane and mesitylene (1 : 3, 5 mL) and an aqueous solution of acetic acid (6 M, 0.4 mL). The tube was degassed through several freeze/pump/thaw cycles and then heated at 120 °C. After 72 h, the mixture was cooled to room temperature, producing a solid that was filtered off and washed several times sequentially with 1,4-dioxane, MeOH, acetone, and THF. The **TFPB–DHTH** COF (92% yield) was obtained as a yellow-brownish solid after drying under vacuum at 120 °C for 24 h (Scheme 2).

Preparation and fluorescence tests of TFPB–DHTH COF solutions. Aqueous solutions of the **TFPB–DHTH** COF were prepared by dissolving it in water or 1× PBS buffer at a concentration of 0.125 mg mL^{-1} through sonication for 2 h. The stock aqueous solutions were stored in a refrigerator at 5 °C until required. Organic solutions of the **TFPB–DHTH** COF were prepared by suspending it in various organic solvents at a concentration of 0.125 mg mL^{-1}, sonicating the mixtures for 2 h, and then subjecting the suspended solutions to centrifugation at 6000 rpm for 20 min; the supernatants containing the well-dissolved **TFPB–DHTH** COF were isolated and stored in a refrigerator at 5 °C until required. For the fluorescence tests, the samples were irradiated at an excitation wavelength of 365 nm, with an emission slit width of 2.5 nm and an excitation slit width of 2.5 nm, under a scan speed of 1200 nm min^{-1}. The resulting emission wavelength was recorded from 200 to 800 nm.

Fluorescence quenching of TFPB–DHTH COF in the presence of Cu^{2+} ions. To examine the effect of Cu^{2+} ions on the fluorescence of the COF, an aqueous solution (0.1 mL) of copper acetate [$Cu(OAc)_2$], copper nitrate [$Cu(NO_3)_2$], or copper chloride ($CuCl_2$), at a final concentration of 200 μM, was added to an aqueous solution of **TFPB–DHTH** COF in 1× PBS (pH 7.4, 0.9 mL) at a final concentration of 0.125 mg mL^{-1}. The mixture was shaken vigorously using a shaker and equilibrated at room temperature for 15 min. The fluorescence emission spectrum of the mixture was recorded. For the sensitivity test, aqueous $CuCl_2$ solutions (0.1 mL) of various concentrations were added to an aqueous solution of **TFPB–DHTH** COF in 1× PBS (pH 7.4, 0.9 mL) at a final concentration of 0.125 mg mL^{-1}. After shaking and 15 min of equilibration, fluorescence emission spectra of the mixtures were measured. For the selectivity test, aqueous solutions (0.1 mL) of various metal ions at a final concentration of 200 μM were added to an aqueous solution of **TFPB–DHTH** COF in 1× PBS (pH 7.4, 0.9 mL) at a final concentration of 0.125 mg mL^{-1}. After shaking of the mixture and 15 min of equilibration, fluorescence emission spectra were recorded.

Fluorescence sensing of Cys and L-His. A stock aqueous solution of Cu@**TFPB–DHTH** COF was prepared through the addition of 0.87 mM aqueous $CuCl_2$ (4.6 mL) to an aqueous solution of **TFPB–DHTH** COF in 1× PBS (pH 7.4, 15.4 mL) at a concentration of 0.162 mg mL^{-1}. The mixture was shaken strongly using a shaker and equilibrated at room temperature for 60 min. The final concentrations of $CuCl_2$ and **TFPB–DHTH** COF were 200 μM and 0.125 mg mL^{-1}, respectively. For the detection of Cys, aqueous solutions of Cys in 1× PBS (pH 7.4, 0.25 mL) of various concentrations were added to the stock solution of Cu@**TFPB–DHTH** COF (0.9 mL) and 2 mM Ni^{2+} (0.12 mL). Each mixture was shaken vigorously and equilibrated at room temperature for 15 min before measuring its fluorescence emission spectrum. For the detection of L-His, aqueous L-His solutions (0.25 mL) of various concentrations were added to the stock solution of Cu@**TFPB–DHTH** COF (0.9 mL) and of 2 mM NEM (0.1 mL). Each mixture was shaken vigorously and equilibrated at room temperature for 15 min before recording its fluorescence emission spectrum. For selectivity tests, other essential amino acids—alanine (Ala), aspartic acid (Asp), glutamine (Gln), glycine (Gly), glutamic acid (Glu), lysine (Lys), phenylalanine (Phe), tryptophan (Trp), proline (Pro), valine (Val), and tyrosine (Tyr)—were tested individually.

Results and discussion

Scheme 1a displays the synthesis of our new **TFPB–DHTH** COF. The use of solvothermal conditions with **TFPB–3CHO** and DHTH in 1,4-dioxane and mesitylene (1 : 3, v/v), in the presence of a catalytic amount of acetic acid (6 M), produced **TFPB–DHTH** COF. Fourier transform infrared (FTIR) and solid state ^{13}C nuclear magnetic resonance (NMR) spectroscopy verified the molecular structure of the **TFPB–DHTH** COF. The FTIR spectrum of DHTH featured a very broad signal in the range 3670–3307 cm^{-1} for the vibrations of the OH groups, overlapped with signals at 3397 and 3307 cm^{-1} for the vibrations of the hydrazide ($NHNH_2$) group, a signal at 1630 cm^{-1} for the vibrations of the amide carbonyl (NHCO) group, and signals

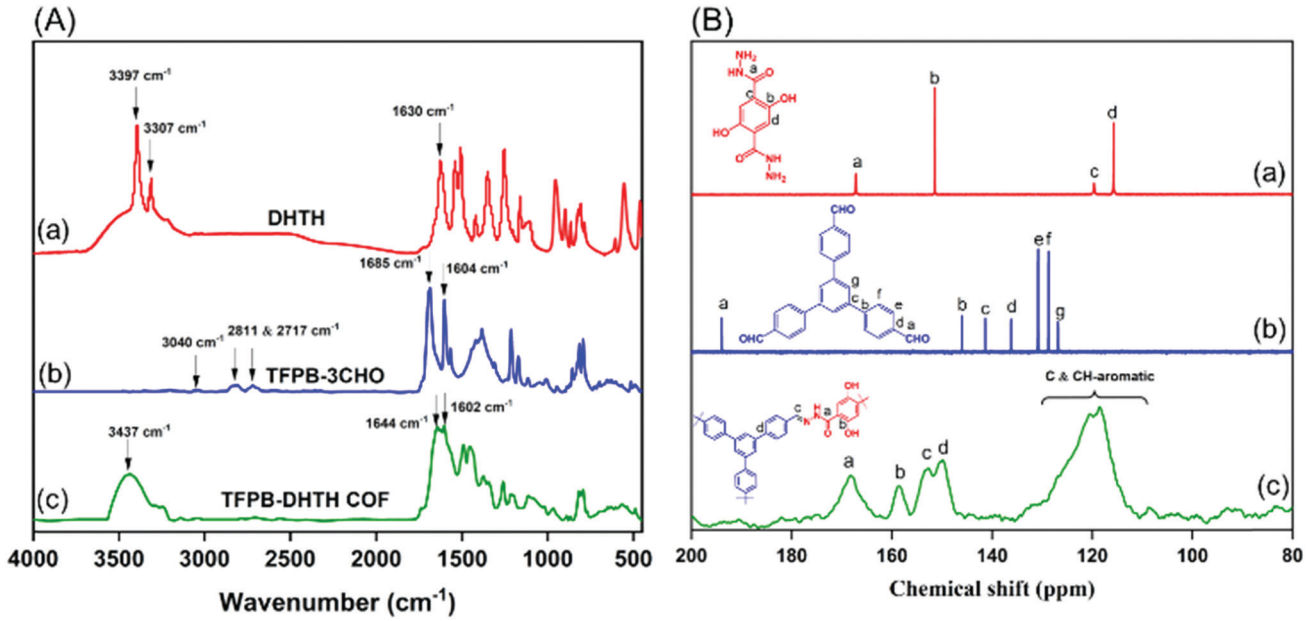

Fig. 1 (A) FTIR spectra of (a) **DHTH**, (b) **TFPB–3CHO**, and (c) the **TFPB–DHTH** COF. (B) ^{13}C NMR spectra of (a) **DHTH** and (b) **TFPB–3CHO** and (c) the solid state ^{13}C NMR spectrum of the **TFPB–DHTH** COF.

at 1613 and 1537 cm^{-1} for the vibrations of aromatic (C═C) bonds [Fig. 1A(a) and Fig. S1, ESI†]. The FTIR spectrum of the triformyl monomer **TFPB–3CHO** featured signals at 3040, 2811, 2717, 1685, and 1605 cm^{-1} for the vibrations of the aromatic C–H bonds, the Fermi double-resonance of the aldehydic C–H bonds, the aldehydic C═O bonds, and the aromatic groups, respectively [Fig. 1A(b) and Fig. S4, ESI†]. The FTIR spectrum of the **TFPB–DHTH** COF did not feature the signals of the aldehydic C–H bonds (at 2811 and 2717 cm^{-1}) nor the aldehydic C═O groups (at 1685 cm^{-1}) of **TFPB–3CHO**, nor the signals of the $NHNH_2$ groups (at 3397 and 3307 cm^{-1}) of DHTH, suggesting complete consumption of these monomers. Moreover, new signals appeared at 1644 and 1602 cm^{-1} for the vibrations of the C═O and C═N groups, respectively, consistent with the formation of the acylhydrazone Schiff base (CONH–N═C) linkages and then the successful formation of the **TFPB–DHTH** COF [Fig. 1A(c)].

The ^{13}C NMR spectrum of DHTH [Fig. 1B(a) and Fig. S3, ESI†] featured a signal at 167.37 ppm representing the carbon nuclei of its C═O groups, as well as a high-intensity signal at 151.50 ppm for the aromatic carbon nuclei attached to the hydrazide group (C–$CONHNH_2$). 7:25 PMhe signals of other aromatic carbon nuclei appeared at 119.73 and 115.59 ppm. The ^{13}C NMR spectrum of **TFPB–3CHO** exhibited a peak at 194.14 ppm representing its aldehydic carbon nuclei [C(═O)–H], as well as signals in the range from 146.07 to 128.86 ppm for the aromatic carbon nuclei [Fig. 1B(b) and Fig. S6, ESI†]. Solid state ^{13}C NMR spectroscopy confirmed the successful condensation between DHTH and **TFPB–3CHO** to form the **TFPB–DHTH** COF, with the disappearance of the signal for the aldehydic carbon nuclei (at 194.14 ppm) of **TFPB–3CHO** and the appearance of new signals at 168.26 and 152.38 ppm for the C═O and C═N groups, respectively, of the formed acylhydrazone Schiff base (CONH–N═C) [Fig. 1B(c)], in addition to signals of the other aromatic carbon nuclei at 158.38, 149.68, and 130.22–110.93 ppm.

To study the crystal structure of the **TFPB–DHTH** COF, we recorded its powder X-ray diffraction (PXRD) pattern with angles 2θ ranging from 1 to 30°. The as-synthesized **TFPB–DHTH** COF featured an experimental pattern (Fig. 2a, black curve) with an intense peak at a value of 2θ of 2.16°, corresponding to the [100] plane. In addition, the PXRD pattern of the COF featured a set of reflected peaks at low-angle range, at values of 2θ of 3.79, 4.40, and 5.83°, that we attribute to its [110], [200], and [210] planes, respectively. In the high-angle region, a broad reflected peak appeared at a value of 2θ of 25.74°, matching the [001] plane (Fig. 2a). This experimental PXRD pattern confirmed that our **TFPB–DHTH** COF possessed a microcrystalline framework and a long-range arrangement. We applied the Bragg equation to calculate the *d*-spacing between the [100] planes (d_{110}) and the interlayer distance between the packed layers of the **TFPB–DHTH** COF. The as-synthesized COF exhibited a value of d_{100} and an interlayer distance of 4.01 nm and 3.45 Å, respectively (Table S1, ESI†). To gain insight into the two-dimensional (2D) packing of the **TFPB–DHTH** COF, we applied Material Studio software to simulate two possible crystalline packing models (completely eclipsed AA-stacking and staggered AB-stacking succession models) of our COF (Fig. 2b, c and Fig. S7, ESI†), and then estimated the theoretical PXRD patterns of these models. Notably, the locations of the experimental PXRD peaks of the **TFPB–DHTH** COF (Fig. 2a, black curve) matched well with those of the simulated PXRD pattern generated through Pawley refinement of the completely eclipsed AA-stacking model of our COF (Fig. 2a, red dots). This matching was confirmed by negligible differences (Fig. 2a, blue curve) between the

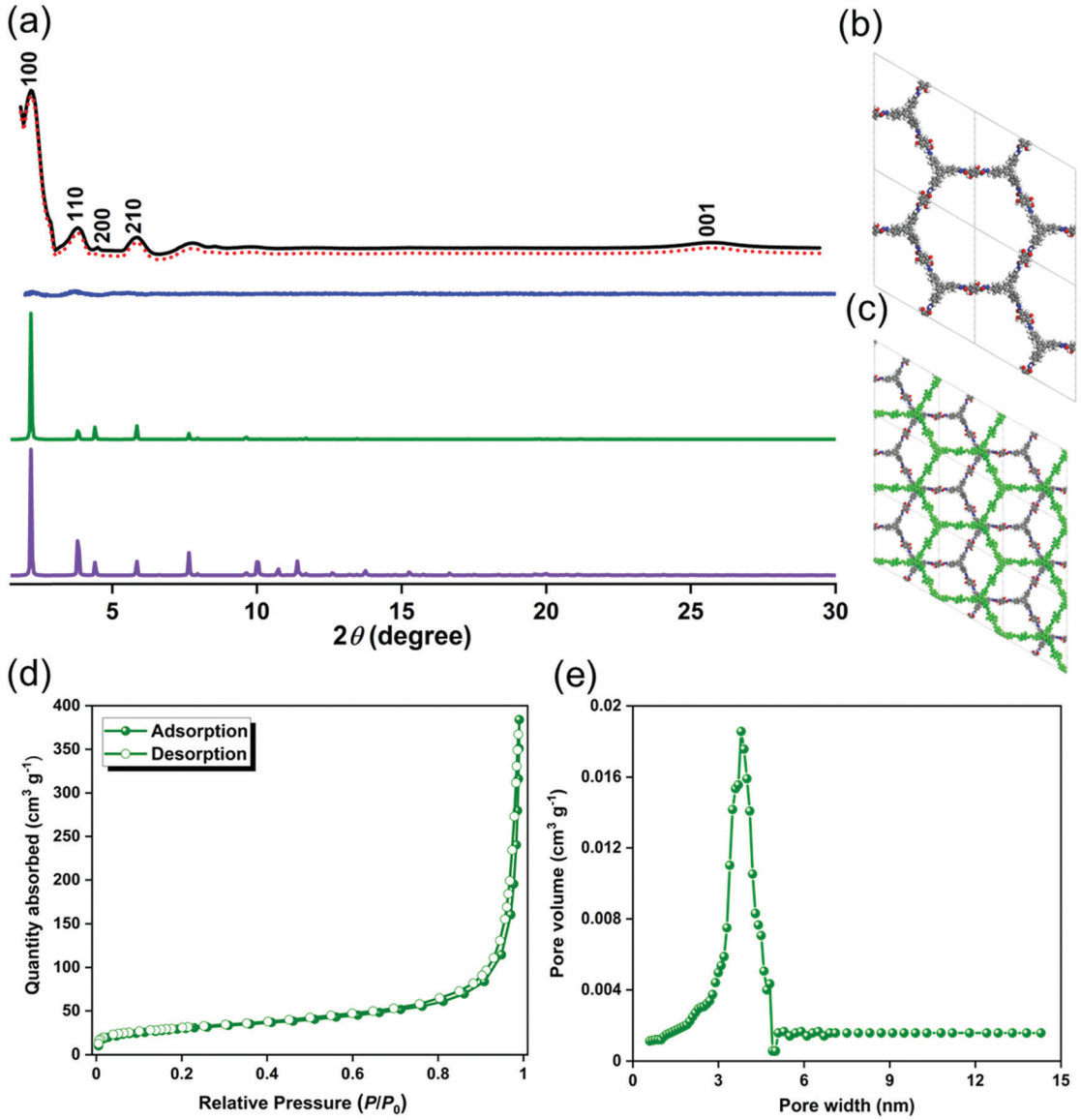

Fig. 2 (a) PXRD patterns of the **TFPB–DHTH** COF: experimental pattern (black); simulated Pawley refined pattern (red dots); their difference pattern (blue); and simulated patterns for the completely eclipsed AA-stacking (olive) and staggered AB-stacking (violet) succession models. (b and c) Top views of (b) the completely eclipsed AA-stacking and (c) staggered AB-stacking succession models. (d) Nitrogen adsorption–desorption isotherm of the **TFPB–DHTH** COF at 77 K. (e) Pore size distribution of the **TFPB–DHTH** COF.

experimental and simulated PXRD patterns. The optimized unit cell parameters of the **TFPB–DHTH** COF, estimated from this refinement of the eclipsed AA-stacking model, were $a = b =$ 46.231 Å, c = 4.078 Å, $\alpha = \beta = 90^\circ$, and $\gamma = 120^\circ$ (Fig. 2b and Fig. S7a and S7b, Table S2, ESI†). Furthermore, comparisons of the experimental PXRD pattern of our **TFPB–DHTH** COF (Fig. 2a, black curve) with the calculated PXRD patterns of the completely eclipsed AA-stacking (Fig. 2a, green curve) and staggered AB-stacking (Fig. 2a, purple curve) succession models revealed consistency with the completely eclipsed AA-stacking model and high variance with the staggered AB-stacking model, suggesting completely eclipsed AA-stacking of the 2D layers in our **TFPB–DHTH** COF.

We measured N_2 gas adsorption and desorption at 77 K to study the porous characteristics of our **TFPB–DHTH** COF. Fig. 2d reveals that the N_2 adsorption curve of the **TFPB–DHTH** COF exhibited a maximum adsorption of 386 $cm^3\ g^{-1}$. We estimated the surface area (360 $m^2\ g^{-1}$) and total pore volume (0.58 $cm^3\ g^{-1}$) of the **TFPB–DHTH** COF from its adsorption/desorption curve, by applying the Brunauer–Emmett–Teller (BET) model. In addition, we used nonlocal density functional theory (NLDFT) to investigate the pore size of the **TFPB–DHTH** COF, validating a narrow pore size distribution with a pore width of 3.77 nm (Fig. 2e and Table S1, ESI†). We visualized the morphology of the **TFPB–DHTH** COF by using FE-SEM and TEM. Fig. S8 (ESI†) reveals that the crystalline **TFPB–DHTH** COF underwent self-assembly during its formation to produce uniform micrometer-scale tubules. Almost all of these **TFPB–DHTH** COF tubules were assembled into a set of bundles,

presumably arising because of strong hydrogen bonding among the surfaces of the COF. Nevertheless, after sonication in polar protic solvents (*e.g.*, EtOH), separated COF tubules could be observed. TEM imaging of the **TFPB–DHTH** COF confirmed the micrometer-scale tubular morphology of our COF; it also revealed that the average length and diameter of the tubular **TFPB–DHTH** COF were 295 ± 32 and 750 ± 45 nm, respectively (Fig. S9, ESI†).

We used thermogravimetric analysis (TGA) to investigate the thermal and chemical stability of our synthesized **TFPB–DHTH** COF. Fig. S10 (ESI†) reveals that the **TFPB–DHTH** COF exhibited sufficient thermal stability, with decomposition temperatures (T_{d10}) of 322 and 321 °C under N_2 and air atmospheres, respectively. In addition, we tested the chemical stability of our **TFPB–DHTH** COF by dispersing 20 mg of the as-synthesized COF in various solvents [1,4-dioxane, THF, acetone, aqueous KOH (1 M), aqueous HCl (1 M), MeOH, DMF, water, and 1× PBS buffer] for 2 days, collecting the solid through filtration under vacuum, washing the sample several times with THF, and finally drying it at 100 °C for 20 h. The PXRD patterns and N_2 gas adsorption and desorption isotherms of the collected COF samples revealed the high chemical stability of the **TFPB–DHTH** COF in these organic and aqueous solvents, as they revealed no changes in the intensities or positions of the signals (Fig. S11, ESI†) in addition to approximate similar surface area values (Table S3, ESI†). We attribute the high thermal stability of the **TFPB–DHTH** COF to the strong intramolecular hydrogen bonds between the C═O groups of the hydrazone Schiff base (CONH–N═C) units and the OH groups in the *ortho* positions of the aromatic rings; we suspected that these units would also act as bidentate sites for the selective bonding of metal ions.

We investigated the electronic excitation and luminescence of the **TFPB–DHTH** COF by measuring its fluorescence emission spectrum in various solvents. We prepared solutions of our COF crystallites in water at concentrations of 0.5, 0.25, 0.125, and 0.0625 mg mL^{-1}, and then excited these solutions at 365 nm. Fig. 3a reveals that the fluorescence spectrum of each aqueous solution of the **TFPB–DHTH** COF exhibited an intense emission maximum at 520 nm. Interestingly, the fluorescence intensity of our COF increased from 16,430 to 31,161 to 41,453 a.u. upon decreasing the concentration of the COF from 0.5 to 0.25 to 0.125 mg mL^{-1} (Fig. 3b), respectively, indicative of aggregation-caused quenching (ACQ) of the **TFPB–DHTH** COF. We attribute the decrease in the fluorescence intensity to 29 677 a.u. at a concentration of our COF of 0.0625 mg mL^{-1} to the very low

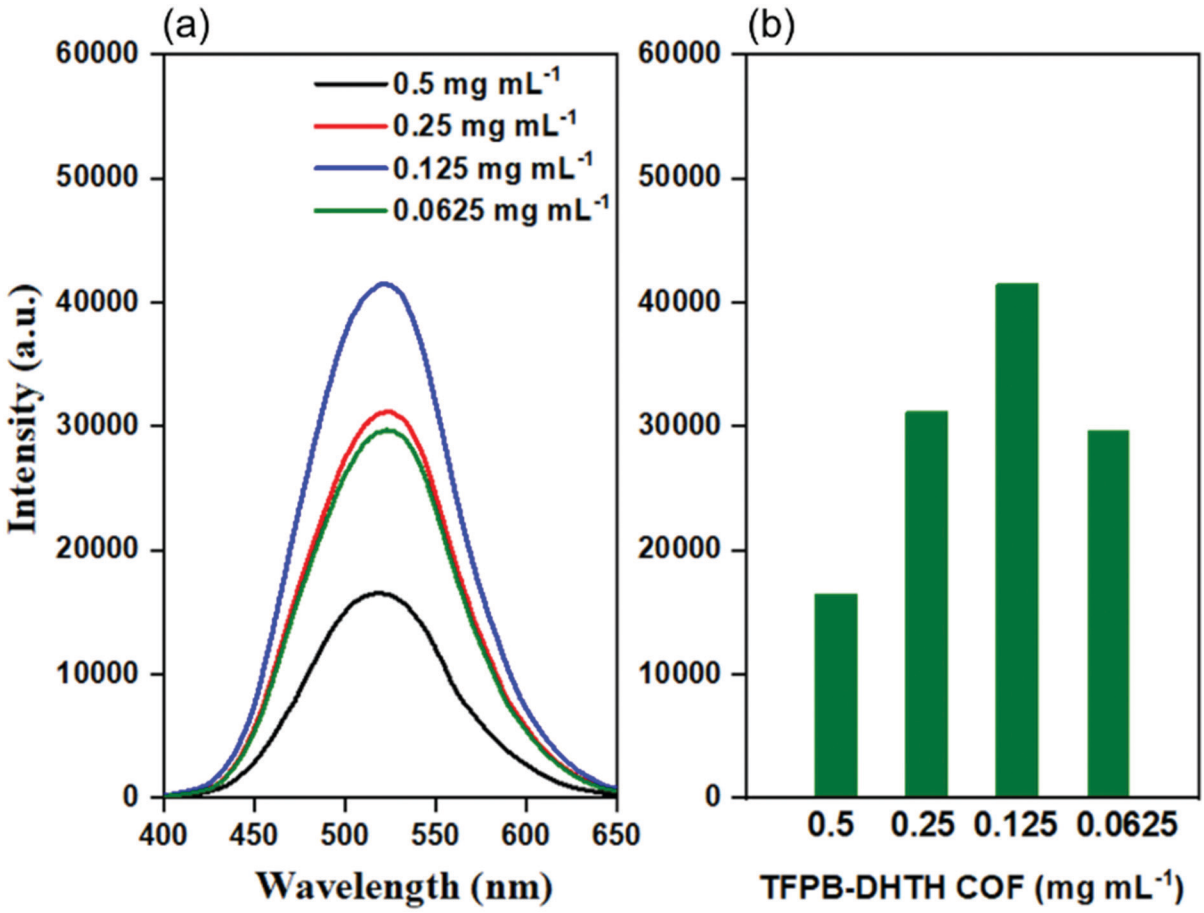

Fig. 3 (a) Fluorescence emission spectra and (b) fluorescence emission intensities at a wavelength of 520 nm of the **TFPB–DHTH** COF dissolved in water at various concentrations (excitation at 365 nm).

amount of **TFPB–DHTH** COF in solution. Recently, we reported that fluorescent COFs having extended conjugated aromatic systems can display significant fluorescence emissions as dilute solutions; in contrast, in solution at high concentrations, their fluorescence emissions are normally quenched through the ACQ phenomenon.[57] Furthermore, we recoded the time-dependent fluorescence intensity of an aqueous solution of **TFPB–DHTH** COF at a concentration of 0.125 mg mL^{-1} over a 60 min period; the maintained intensity suggested that our **TFPB–DHTH** COF did not display any photo-bleaching (Fig. S12, ESI†). We also studied the fluorescence behavior of the **TFPB–DHTH** COF in various solvents—THF, 1,4-dioxane, acetone, MeOH, DMF, water, and 1× PBS buffer (pH 7.4)—at a recording concentration of 0.0625 mg mL^{-1}. The excitation of our COF solutions in THF, 1,4-dioxane, and acetone, using light from a common UV lamp at a wavelength of 365 nm, resulted in very weak (nearly dark) fluorescence colors that were clear to the naked eye (Fig. 4a). In contrast, the solutions of **TFPB–DHTH** COF in MeOH, DMF, water, and 1× PBS buffer displayed extremely bright yellow fluorescence. We also used a fluorescence spectrometer to record the fluorescence emission spectra of our COF in the same solvents under an excitation wavelength of 365 nm and open to the atmosphere. Fig. 4b reveals that the fluorescence spectra of the **TFPB–DHTH** COF in MeOH, DMF, water, and 1× PBS buffer show high-intensity emission maxima at 509, 512, 520, and 520 nm, respectively; in THF, 1,4-dioxane, and acetone they exhibited very weak emission maxima at 450, 449, and 502 nm, respectively. Thus, the emission wavelength of our COF was strongly influenced by the polarity of the solvent; upon increasing the polarity, the emission wavelength red-shifted. We attribute this solvatochromic effect of the emission wavelength of the **TFPB–DHTH** COF to strong noncovalent interactions (*e.g.*, dipole effects, hydrogen bonding) between the COF and the solvent molecules of MeOH, DMF, water, and 1× PBS buffer, resulting in the stabilization of the excited state of the **TFPB–DHTH** COF and, therefore, facilitated charge-transfer. The absolute PLQY of our new COF in water, where it displayed very high fluorescence, was 22.6%. Furthermore, we estimated the band gap and the energy of the highest occupied molecular orbital (HOMO) of our new **TFPB–DHTH** COF by using UV-Vis absorption and photoelectron spectrometry. The UV-Vis spectrum of the **TFPB–DHTH** COF featured a characteristic band having its maximum

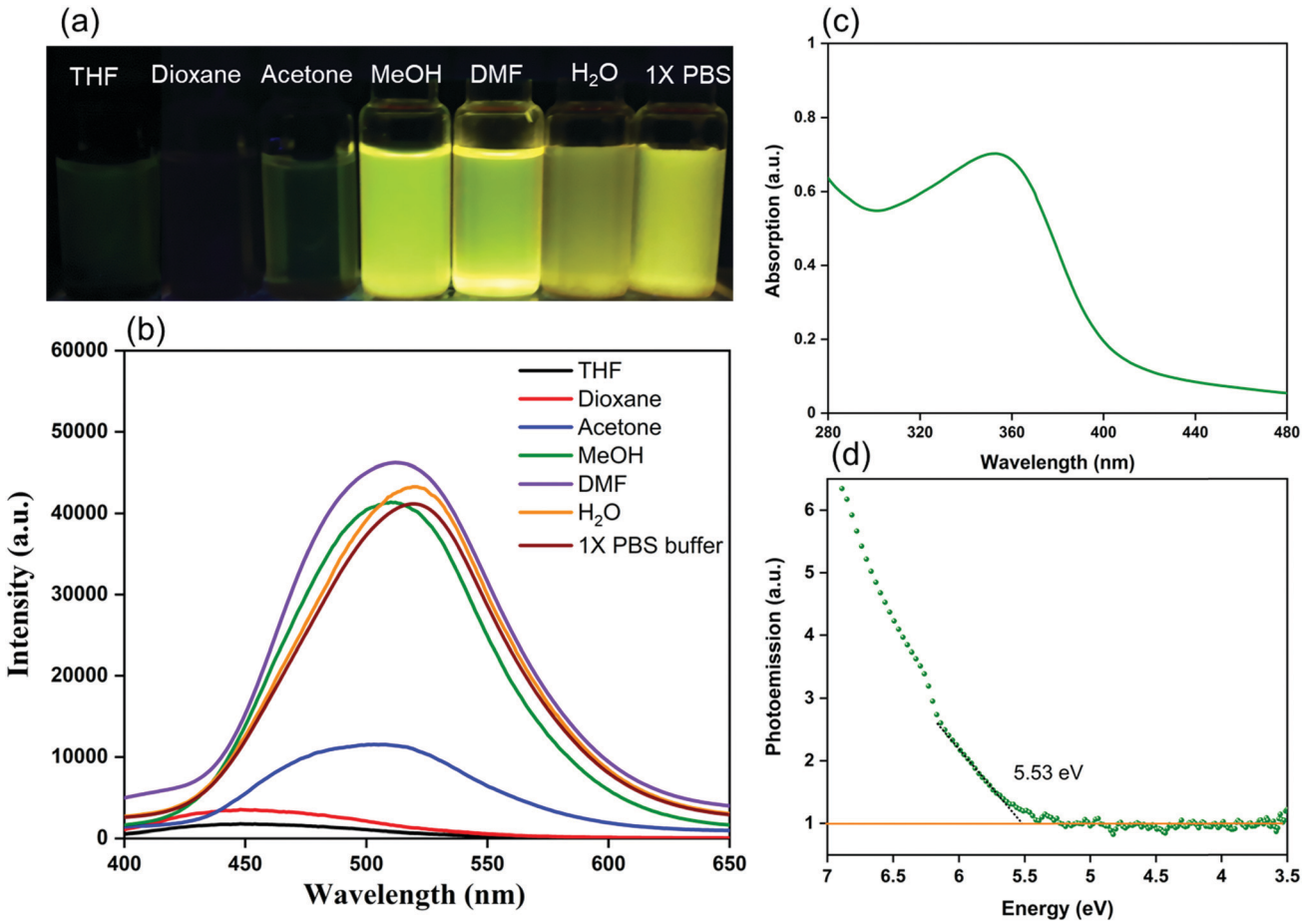

Fig. 4 (a) Photographic images of the **TFPB–DHTH** COF dissolved/dispersed in various solvents upon irradiation with UV light at 360 nm. (b) Fluorescence emission spectra of the **TFPB–DHTH** COF dissolved/dispersed in various solvents (excitation at 365 nm). (c) UV-Vis absorption spectrum of the **TFPB–DHTH** COF dissolved in water (concentration: 0.125 mg mL^{-1}). (d) Photoelectron spectroscopy of the **TFPB–DHTH** COF for calculation of the HOMO energy.

adsorption at 354 nm (Fig. 4c). Converting the UV-Vis spectrum of our COF into a Tauc plot (Fig. S13, ESI†) revealed that the band gap of our **TFPB–DHTH** COF was 3.16 eV. The photoelectron spectrum of the **TFPB–DHTH** COF revealed a HOMO energy of 5.53 eV (Fig. 4d). Finally, we determined the energy of the lowest unoccupied molecular orbital (LUMO) of our **TFPB–DHTH** COF to be 2.37 eV, by subtracting the band gap from the HOMO energy.

Our new **TFPB–DHTH** COF displayed a high fluorescence emission, a uniform distribution of acylhydrazone and OH groups, excellent crystallinity, and good solubility in water and buffer; therefore, we were encouraged to investigate its applications for fluorescence sensing. First, we evaluated the quenching effect of the **TFPB–DHTH** COF dissolved in 1× PBS buffer (pH 7.4) after the addition of copper (Cu^{2+}) ions. We added aqueous solutions of copper salts with different counter ions [$Cu(OAc)_2$, $Cu(NO_3)_2$, $CuCl_2$] to a solution of **TFPB–DHTH** COF in water. Fig. 5a reveals that the fluorescence emission intensity of the **TFPB–DHTH** COF was quenched dramatically after the addition of these copper salts. The approximately equal quenching efficiencies upon the addition of these copper salts suggested that the counter anions (OAc^-, NO_3^-, Cl^-) had only marginal effects on the recognition of the Cu^{2+} ions by the **TFPB–DHTH** COF.

We investigated the selective quenching of the fluorescence of the **TFPB–DHTH** COF by Cu^{2+} ions by observing the change in the fluorescence emission intensity of our COF in the presence of 12 different metal ions (MCl_x; M^{x+} = Na^+, Li^+, Ag^+, Mg^{2+}, Ba^{2+}, Zn^{2+}, Ca^{2+}, Al^{3+}, Cr^{3+}, Fe^{2+}, Fe^{3+}, Hg^{2+}, Cu^{2+}) (Fig. 5b). Among these tested metal ions, only Cu^{2+} ions caused strong quenching of the fluorescence of the **TFPB–DHTH** COF;

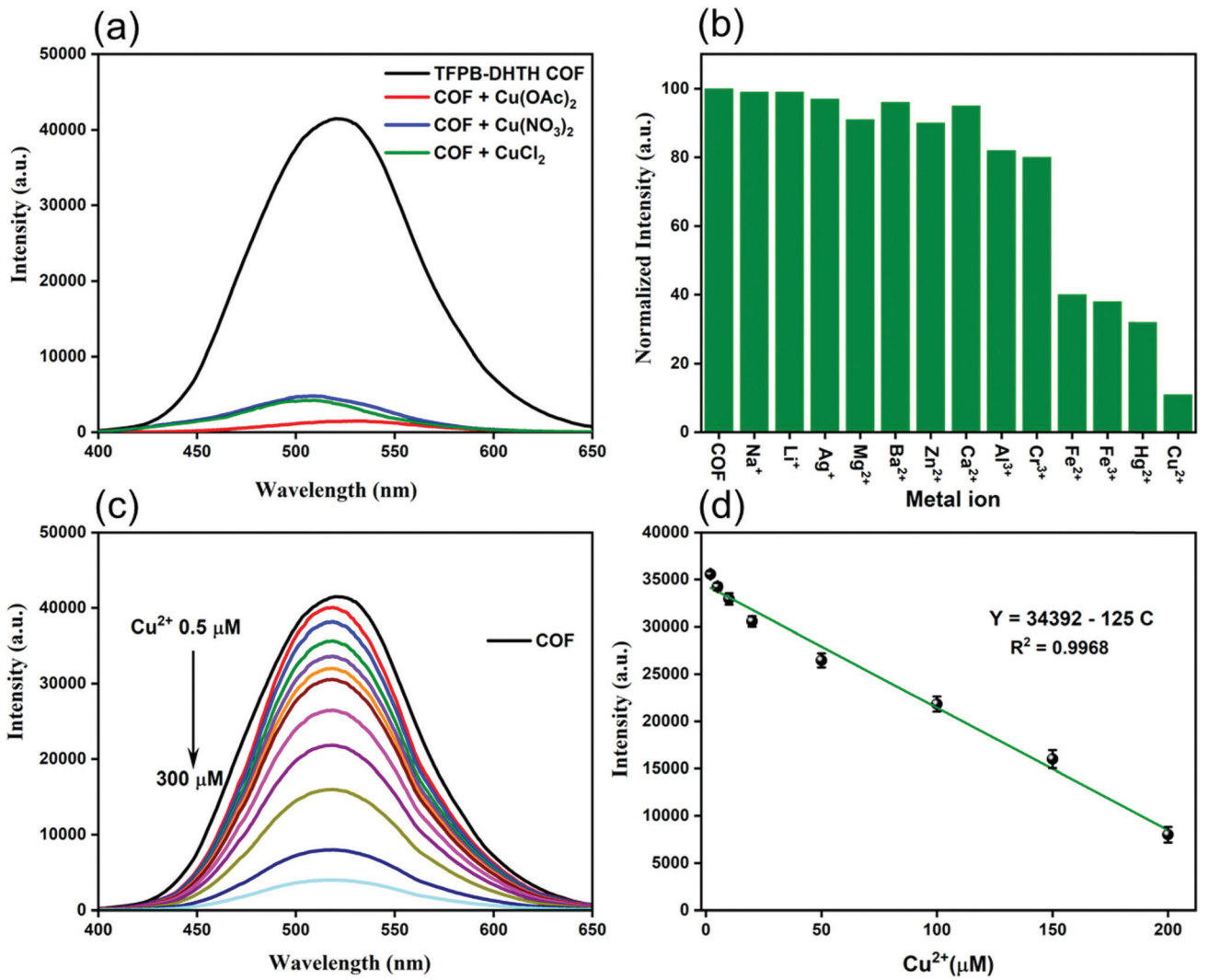

Fig. 5 (a) Fluorescence emission spectra of the **TFPB–DHTH** COF dissolved in 1× PBS buffer (pH 7.4) in the presence of copper salts having various counter ions (Cu^{2+} concentration: 200 μM). (b) Fluorescence emission intensities at a wavelength of 520 nm of the **TFPB–DHTH** COF dissolved in 1× PBS buffer (pH 7.4) in the presence of Cu^{2+} and other metal ions (metal ion concentration: 200 μM). (c) Fluorescence emission spectra of the **TFPB–DHTH** COF dissolved in 1× PBS buffer (pH 7.4) in the presence of various concentrations of Cu^{2+} ions. (d) Calibration curve of the fluorescence emission intensity of the **TFPB–DHTH** COF with respect to the concentration of Cu^{2+} ions. Measurements were made at a **TFPB–DHTH** COF concentration of 0.125 mg mL^{-1} and under excitation at 365 nm.

the other metal ions had only slight fluorescence quenching effects. Alkali metal ions (Na^+, Li^+, Ag^+), alkaline earth ions (Mg^{2+}, Ba^{2+}, Ca^{2+}), and the transition metal Zn^{2+} ion had negligible effects on the fluorescence emission intensity of our COF; Al^{3+} and Cr^{3+} ions quenched approximately 10% of the fluorescence intensity, while the Fe^{2+}, Fe^{3+}, and Hg^{2+} ions both quenched it by approximately 60%. These findings confirmed the outstanding selectivity and excellent quenching response of our **TFPB–DHTH** COF toward Cu^{2+} ions, with a quenching efficiency of approximately 90% (Fig. 5b). To optimize the fluorescence quenching with Cu^{2+} ions, we evaluated the fluorescence emission intensity of our COF in water in the presence of $CuCl_2$ at various concentrations in 1× PBS buffer (pH 7.4). Fig. 5c reveals that the fluorescence emission intensity of an aqueous solution of **TFPB–DHTH** COF at a concentration of 0.125 mg mL^{-1} decreased gradually upon increasing the concentration of Cu^{2+} ions from 0.5 to 200 μM, but remained nearly unaffected thereafter when the concentration of Cu^{2+} ions increased to 300 μM. Approximately 90% of the fluorescence emission intensity of our COF was quenched in the presence of 200 μM of Cu^{2+} ions, representing a mole ratio of 1 : 6.8 (**TFPB–DHTH** COF/Cu^{2+}). Thus, full quenching of the fluorescence of **TFPB–DHTH** COF required at least 6 mole equivalents of Cu^{2+} ions. The fluorescence emission of the COF and the concentration of Cu^{2+} ions had a linear relationship in the range from 2 to 200 μM, characterized by the equation $Y = 34\,392 - 125C$, where Y is the fluorescence intensity and C is the concentration of Cu^{2+} ions in solution; the correlation coefficient (R^2) was 0.968 (Fig. 5d). We estimated the limit of detection (LOD) of Cu^{2+} ions to be 12 nM, based on $3\sigma/k$ (where σ is the standard deviation of six blanks and k is the slope of the calibration curve). The Cu^{2+} ion has significant coordination ability toward fluorescent materials and COFs having amino, C═O, and OH groups in their structures; this coordinative binding induces electron transfer from the excited state of the fluorescent materials and COFs to the Cu^{2+} ion, leading to a dramatic quenching of fluorescence.[69–73] Similarly, we attribute the fluorescence quenching of our **TFPB–DHTH** COF to strong binding between Cu^{2+} ions and the active sites (C═O and OH groups) in the pore walls of our COF. This binding would induce electron transfer from the excited state of the COF to the Cu^{2+} ions. This electron transfer process and the coordination interaction between Cu^{2+} ions and the **TFPB–DHTH** COF were confirmed by X-ray photoelectron spectroscopy (XPS) measurements. Fig. S14 (ESI†) reveals that the **TFPB–DHTH** COF featured a set of XPS peaks of C1s, N1s, and O1s, while Cu@**TFPB–DHTH** COF featured a Cu2p peak in addition to other XPS peaks of C1s, N1s, and O1s. Fig. S15a and b (ESI†) also reveals that the binding energy of O1s orbital shifted from 532.37 eV in **TFPB–DHTH** COF to 533.26 eV in Cu@**TFPB–DHTH** COF. This positive shifting, therefore, strongly confirms the electron-transfer process from the excited state of the COF to the Cu^{2+} ions *via* the donor–acceptor coordination bonds formed between the active sites (C═O and OH groups) in **TFPB–DHTH** COF and Cu^{2+} ions. Moreover, the Cu2p peak reveals $Cu2p_{1/2}$ and $Cu2p_{3/2}$ orbitals 954.24 and 934.71 eV, respectively (Fig. S15c, ESI†). Because we obtained 90% quenching of the fluorescence intensity of the aqueous COF solution (0.125 mg mL^{-1}) upon the addition of 200 μM of Cu^{2+} ions, we prepared a corresponding stock solution of the Cu@**TFPB–DHTH** COF to test the turn-on fluorescence sensing of Cys and L-His.

The thiol functional groups of two Cys moieties can undergo coordination with a Cu^{2+} ion to form a stable 2 : 1 Cys/Cu^{2+} complex. The thiol–Cu^{2+} interaction is relatively stronger than the coordination between a Cu^{2+} ion and C═O, OH and amino groups.[71,74,75] In addition, the imidazole group of L-His can interact strongly with a Cu^{2+} ion to produce a stable 2 : 1 L-His/Cu^{2+} complex; again, the binding affinity is higher than that between a Cu^{2+} ion and C═O, OH, and amino groups.[71,74] Consequently, we suspected that addition of Cys or L-His to the Cu@**TFPB–DHTH** COF might induce snatching and seizure of its Cu^{2+} ions, thereby switching on the fluorescence emission of our **TFPB–DHTH** COF.

Therefore, we tested the Cu@**TFPB–DHTH** COF assembly as an ''OFF–ON'' fluorescence probe for the detection of Cys and L-His, operating through competitive coordination among the **TFPB–DHTH** COF, Cu^{2+} ions, and Cys/L-His influencing the fluorescence emission of the **TFPB–DHTH** COF. To determine the optimal conditions for the ''OFF–ON'' fluorescence detection of Cys and L-His, we varied the pH and the incubation time. Fig. S16a and S16c (ESI†) reveal that the fluorescence emission intensity of the aqueous solution of the Cu@**TFPB–DHTH** COF was recovered maximally, after the addition of aqueous solution of Cys (400 μM) or L-His (500 μM), for values of pH in the range from 4 to 7.4. Therefore, we selected pH 7.4, suitable for biological systems, as the optimal pH for the detection of Cys and L-His. Fig. S16b and S16d (ESI†) reveal the relationship between the fluorescence recovery intensity and the incubation time. The fluorescence intensity reached a maximum when the incubation time approached 15 min and then remained constant thereafter. Therefore, for subsequent detection of Cys and L-His, we employed an incubation time of 15 min.

Under these optimal conditions, we evaluated the ''OFF–ON'' fluorescence detection of Cys and L-His and examined the relationship between the fluorescence recovery intensity and the concentration of Cys and L-His. For Cys, the intensity of the fluorescence emission peak at 520 nm increased upon increasing of the concentration of Cys in the range from 2 to 400 μM in the presence of 300 μM of Ni^{2+} ions; it did not change any more upon increasing the concentration of Cys thereafter to 500, 1000, or 1500 μM (Fig. 6a and b). The inset of Fig. 6b reveals a linear relationship between the fluorescence intensity at 520 nm and the Cys concentration over the range from 2 to 100 μM. The regression equation for Cys detection was I = 8126.21 + 221.76[Cys], where I is the fluorescence intensity at 520 nm and [Cys] is the concentration of Cys (μM); the correlation coefficient (R^2) was 0.9997. The LOD of Cys when using our new ''OFF–ON'' Cu@**TFPB–DHTH** COF fluorescence probe was equal to 340 nM, based on a signal-to-noise value (S/N) of 3. Likewise, upon incremental addition of L-His at concentrations in the range from 2 to 400 μM, the fluorescence intensity of our new Cu@**TFPB–DHTH** COF at 520 nm increased in the presence of 200 μM of NEM. The fluorescence intensity

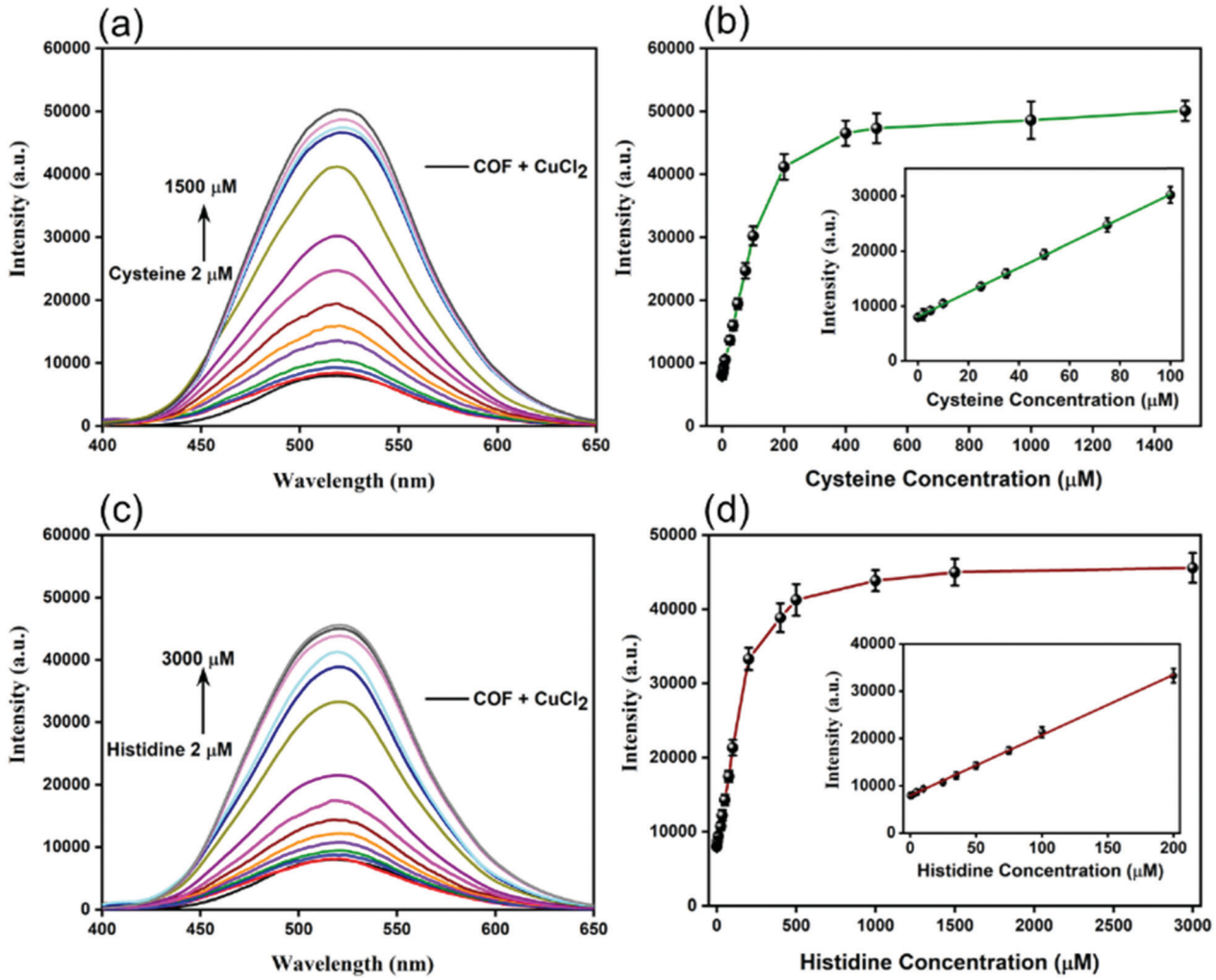

Fig. 6 (a) Fluorescence emission spectra of the Cu@**TFPB–DHTH** COF dissolved in 1× PBS buffer (pH 7.4) in the presence of various concentrations of Cys. (b) Calibration curve of the fluorescence emission intensity of the Cu@**TFPB–DHTH** COF with respect to the concentration of Cys. (c) Fluorescence emission spectra of the Cu@**TFPB–DHTH** COF dissolved in 1× PBS buffer (pH 7.4) in the presence of various concentrations of L-His. (d) Calibration curve of the fluorescence emission intensity of the Cu@**TFPB–DHTH** COF with respect to the concentration of L-His. Measurements were made at concentrations of the Cu@**TFPB–DHTH** COF and the Cu^{2+} ions of 0.125 mg mL^{-1} and 200 μM, respectively, under excitation at 365 nm.

remained approximately unchanged when the concentration of L-His was greater than 500 mM (Fig. 6c and d). The inset of Fig. 6d reveals that the fluorescence intensity at 520 nm exhibited a linear relationship with the concentration of L-His within the range from 2 to 200 μM. The linear curve provided a regression equation for L-His detection of I = 7947.02 + 127.77 [L-His], where I is the fluorescence intensity at 520 nm and [L-His] is the concentration of L-His (μM); the correlation coefficient (R^2) was 0.9993. We calculated the LOD of L-His to be 520 nM. Compared with other reported methods for the detection of Cys and L-His (Table S4, ESI†), our present method is among the most highly selective. In addition, our detection strategy has several advantages over those previous methods, including high thermal and chemical stability, no need for chemical modification, excellent crystallinity, high solubility in water, and low cost.

We examined the selectivity of our new Cu@**TFPB–DHTH** COF as an ''OFF–ON'' fluorescence probe by monitoring its fluorescence response after treatment with 13 different amino acids (Ala, Asp, Gln, Gly, Glu, Lys, Phe, Trp, Pro, Val, Tyr, Cys, L-His), each at a concentration of 200 μM. Fig. S17 (ESI†) reveals that, among the tested amino acids, only Cys and L-His could trigger a considerable recovery of the fluorescence intensity of the Cu@**TFPB–DHTH** COF probe; the other amino acids did not cause any major changes in the fluorescence intensity of our probe. To differentiate between Cys and L-His, we employed Ni^{2+} as a well-established L-His–binding metal ion and NEM as a Cys-masking reagent for the isolation of L-His and Cys, respectively, in our Cu@**TFPB–DHTH** COF–based detection assay. Because the Ni^{2+} ion binds selectively to L-His, we could detect Cys quantitatively when using our Cu@**TFPB–DHTH** COF probe; similarly, we could achieve the quantitative detection of L-His in the presence of NEM. Furthermore, Fig. S17 (ESI†) reveals that the presence of Ni^{2+} ions in the detection system did not affect the fluorescence recovery efficiency of Cys; neither did the presence of NEM affect the

recovery efficiency of L-His. Therefore, our new detection strategy displayed good selectivity toward Cys and L-His, separately.

Conclusions

We have prepared a new fluorescent OH- and hydrazone-functionalized COF (**TFPB–DHTH** COF) displaying high crystallinity, excellent chemical stability, and suitable functional groups for interaction with metal ions; its solutions in water and buffer exhibited very high fluorescence emission under UV irradiation. The fluorescence emission of the **TFPB–DHTH** COF was switched off selectively upon the addition of Cu^{2+} ions, due to electron transfer from the excited state of the COF to the Cu^{2+} ions. The formed Cu@**TFPB–DHTH** COF functioned as an ''OFF–ON'' fluorescent sensor for the specific detection and differentiation of Cys and L-His in the presence of Ni^{2+} ions and NEM, respectively. Our new sensing assay could be completed within 30 min, with LODs of 340 and 520 nM for Cys and L-His, respectively. Thus, this facile ''OFF–ON'' detection assay for Cys and L-His would appear to have significant potential for use in a number of other domains.

Conflicts of interest

There are no conflicts to declare.

Acknowledgements

This study was supported financially by the Ministry of Science and Technology, Taiwan, under contracts MOST 108-2638-E-002-003-MY2 and 108-2218-E-110-013-MY3.

Notes and references

1 Z. H. Fu, X. Han, Y. Shao, J. Fang, Z.-H. Zhang, Y.-W. Wang and Y. Peng, *Anal. Chem.*, 2017, **89**, 1937–1944.
2 H. Zhang, W. Li, J. Chen, G. Li, X. Yue, L. Zhang, X. Song and W. Chen, *Anal. Chim. Acta*, 2020, **1097**, 238–244.
3 H. S. Jung, X. Chen, J. S. Kim and J. Yoon, *Chem. Soc. Rev.*, 2013, **42**, 6019–6031.
4 X. Zhang, J. Lu, X. Ren, Y. Du, Y. Zheng, P. V. Ioannou and A. Holmgren, *Biol. Med.*, 2015, **152**, 192–200.
5 Q. Lin, K. Zhong, J. Zhu, L. Ding, J. Su, H. Yao, T. Wei and Y. Zhang, *Macromolecules*, 2017, **20**, 7863–7871.
6 R. Janáky, V. Varga, A. Hermann, P. Saransaari and S. S. Oja, *Neurochem. Res.*, 2000, **9**, 1397–1405.
7 C. Yee, W. Yang and S. Hekimi, *Cell*, 2014, **4**, 897–909.
8 E. Weerapana, C. Wang, G. M. Simon, F. Richter, S. Khare, M. B. D. Dillon, D. A. Bachovchin, K. Mowen, D. Baker and B. F. Cravatt, *Nature*, 2010, **7325**, 790–795.
9 Y. Bessho, E. Iwakoshi-Ukena, T. Tachibana, S. Maejima, S. Taniuchi, K. Masuda, K. Shikano, K. Kondo, M. Furumitsu and K. Ukena, *Neurosci. Lett.*, 2014, **578**, 106–110.
10 L. D. Li, Z. B. Chen, H. T. Zhao and L. Guo, *Biosens. Bioelectron.*, 2011, **26**, 2781–2785.
11 M. Watanabe, M. E. Suliman, A. R. Qureshi, E. Garcia-Lopez, P. Bárány, O. Heimbürger, P. Stenvinkel and B. Lindholm, *Am. J. Clin. Nutr.*, 2008, **87**, 1860–1866.
12 H. Saito, L. T. Goodnough, J. M. Boyle and N. Heimburger, *Am. J. Med.*, 1982, **73**, 90175–90179.
13 K. V. R. Rao, P. V. B. Reddy, X. Tong and M. D. Norenberg, *Am. J. Pathol.*, 2010, **176**, 1400–1408.
14 H. Li, J. Liu, Y. Fang, Y. Qin, S. Xu, Y. Liu and E. Wang, *Biosens. Bioelectron.*, 2013, **41**, 563–568.
15 Q. Xiao, H. Gao, Q. Yuan, C. Lu and J. Lin, *J. Chromatogr. A*, 2013, **1274**, 145–150.
16 X. Wang, C. Luo, L. Li and H. Duan, *J. Electroanal. Chem.*, 2015, **757**, 100–106.
17 K. B. A. Ahmed, M. Sengan, P. S. Kumar and A. Veerappan, *Sens. Actuators, B*, 2016, **233**, 431–437.
18 C. Song, W. Zhao, H. Liu, W. Ding, L. Zhang, J. Wang, Y. Yao and C. Yao, *J. Mater. Chem. B*, 2020, **8**, 494–7500.
19 Y. Che, H. Pang, H. Li, L. Yang, X. Fu, S. Liu, L. Ding and J. Hou, *Talanta*, 2019, **196**, 442–448.
20 S. Ma, Q. Zhang, D. Wu, Y. Hu, D. Hu, Z. Guo, S. Wang, Q. Liu and J. Peng, *J. Electroanal. Chem.*, 2019, **847**, 113144.
21 R. Shen, L. Zou, S. Wu, T. Li, J. Wang, J. Liu and L. Ling, *Spectrochim. Acta, Part A*, 2019, **213**, 42–47.
22 M. Tian, F. Guo, Y. Sun, W. Zhang, F. Miao, Y. Liu, G. Song, C.-L. Ho, X. Yu, J. Z. Sun and W.-Y. Wong, *Org. Biomol. Chem.*, 2014, **12**, 6128–6133.
23 K. S. Park, M. I. Kim, M. Woo and H. G. Park, *Biosens. Bioelectron.*, 2013, **45**, 65–69.
24 F. Yan, D. Shi, T. Zheng, K. Yun, X. Zhou and L. Chen, *Sens. Actuators, B*, 2016, **224**, 926–935.
25 W. X. Ze, Z. Q. Zhang, R. Guo, Y. Y. Zhang, N. J. Zhu, K. Wang, P. P. Sun, X. Y. Mao, J. J. Liu, J. Z. Huo, X. R. Wang and B. Ding, *Talanta*, 2020, **217**, 121010.
26 J. Wang, H. Jiang, H. Liu, L. Liang and J. Tao, *Spectrochim. Acta, Part A*, 2020, **228**, 117725.
27 L. Zhao, X. He, Y. Huang, S. Zhang, H. Han, L. Xu, X. Wang, D. Song, P. Ma and Y. Sun, *Anal. Bioanal. Chem.*, 2020, **412**, 7211–7217.
28 J. Peng, P. Gong, S. Li, F. Kong, X. Ge, B. Wang, L. Guo, Z. Liu and J. You, *Chem. Eng. J.*, 2020, **391**, 123619.
29 P. Gong, L. Sun, F. Wang, X. Liu, Z. Yan, M. Wang, L. Zhang, Z. Tian, Z. Liu and J. You, *Chem. Eng. J.*, 2019, **356**, 994–1002.
30 P. Gong, S. Ji, J. Wang, D. Dai, F. Wang, M. Tian, L. Zhang, F. Guo and Z. Liu, *Chem. Eng. J.*, 2018, **348**, 438–446.
31 Y. Cai, J. Wang, C. Liu, S. Yang, Y. Zhang and A. Liu, *ChemComm*, 2020, **56**, 11637–11640.
32 D. Sun, T. Liu, C. Wang, L. Yang, S. Yang and K. Zhuo, *Spectrochim. Acta, Part A*, 2020, **240**, 118598.
33 C. Das, B. Pakhira, A. L. Rheingold and S. K. Chattopadhyay, *Inorg. Chim. Acta*, 2018, **482**, 292–298.
34 A. P. Cote, A. I. Benin, N. W. Ockwig, M. O'Keeffe, A. J. Matzger and O. M. Yaghi, *Science*, 2005, **310**, 1166–1170.

35 Y. Li, W. Chen, G. Xing, D. Jiang and L. Chen, *Chem. Soc. Rev.*, 2020, **49**, 2852–2868.
36 S. Yuan, X. Li, J. Zhu, G. Zhang, P. V. Puyvelde and B. V. Bruggen, *Chem. Soc. Rev.*, 2019, **48**, 2665–2681.
37 T. Ma, E. A. Kapustin, S. X. Yin, L. Liang, Z. Zhou, J. Niu, L.-H. Li, Y. Wang, J. Su, J. Li, X. Wang, W. D. Wang, W. Wang, J. Sun and O. M. Yaghi, *Science*, 2018, **361**, 48–52.
38 M. D. Allendorf, C. A. Bauer, R. K. Bhakta and R. J. T. Houk, *Chem. Soc. Rev.*, 2009, **38**, 1330–1352.
39 V. A. Kuehl, J. Yin, P. H. H. Duong, B. Mastorovich, B. Newell, K. D. Li-Oakey, B. A. Parkinson and J. O. Hoberg, *J. Am. Chem. Soc.*, 2018, **140**, 18200–18207.
40 Y. Meng, Y. Luo, J. Shi, H. Ding, X. Lang, W. Chen, A. Zheng, J. Sun and C. Wang, *Angew. Chem., Int. Ed.*, 2020, **59**, 3624–3629.
41 A. F. M. EL-Mahdy, M. B. Zakaria, H. X. Wang, T. Chen, Y. Yamauchi and S. W. Kuo, *J. Mater. Chem. A*, 2020, **8**, 25148–25155.
42 A. F. M. El-Mahdy, C. H. Kuo, A. Alshehri, C. Young, Y. Yamauchi, J. Kim and S. W. Kuo, *J. Mater. Chem. A*, 2018, **6**, 19532–19541.
43 X. Chen, K. Geng, R. Liu, K. T. Tan, Y. Gong, Z. Li, S. Tao, Q. Jiang and D. Jiang, *Angew. Chem., Int. Ed.*, 2020, **59**, 5050–5091.
44 H. R. Abuzeid, A. F. M. EL-Mahdy and S. W. Kuo, *Microporous Mesoporous Mater.*, 2020, **300**, 110151.
45 A. F. M. El-Mahdy, Y. H. Hung, T. H. Mansoure, H. H. Yu, T. Chen and S. W. Kuo, *Asian J. Chem.*, 2019, **14**, 1429–1435.
46 A. F. M. El-Mahdy, C. Young, J. Kim, J. You, Y. Yamauchi and S. W. Kuo, *ACS Appl. Mater. Interfaces*, 2019, **11**, 9343–9354.
47 L. Zhang, S. Wang, Y. Zhou, C. Wang, X. Z. Zhang and H. Deng, *Angew. Chem., Int. Ed.*, 2019, **131**, 14351–14356.
48 A. F. M. EL-Mahdy, Y. H. Hung, T. H. Mansoure, H. H. Yu, Y. S. Hsu, K. C. Wu and S. W. Kuo, *J. Taiwan Inst. Chem. Eng.*, 2019, **103**, 199–208.
49 H. R. Abuzeid, A. F. M. EL-Mahdy, M. M. M. Ahmed and S. W. Kuo, *Polym. Chem.*, 2019, **10**, 6010–6020.
50 W. R. Cui, C. R. Zhang, W. Jiang, F. F. Li, R. P. Liang, J. Liu and J. D. Qiu, *Nat. Commun.*, 2020, **11**, 436.
51 P. Das and S. K. Mandal, *J. Mater. Chem. A*, 2018, **6**, 16246–16256.
52 A. F. M. EL-Mahdy, A. M. Elewa, S. W. Huang, H. H. Chou and S. W. Kuo, *Adv. Opt. Mater.*, 2020, **8**, 2000641.
53 X. Li, Q. Gao, J. Wang, Y. Chen, Z. H. Chen, H. S. Xu, W. Tang, K. Leng, G. H. Ning, J. Wu, Q. H. Xu, S. Y. Queck, Y. Lu and K. P. Loh, *Nat. Commun.*, 2018, **9**, 2335.
54 C. Wu, Y. Liu, H. Liu, C. Duan, Q. Pan, J. Zhu, F. Hu, X. Ma, T. Jiu, Z. Li and Y. Zhao, *J. Am. Chem. Soc.*, 2018, **140**, 10016–10024.
55 B. Wang, X. Liu, P. Gong, X. Ge, Z. Liu and J. You, *ChemComm*, 2020, **56**, 519–522.
56 M. G. Mohamed, C. C. Lee, A. F. M. EL-Mahdy, J. Lüder, M. H. Yu, Z. Li, Z. Zhu, C. C. Chueh and S. W. Kuo, *J. Mater. Chem. A*, 2020, **8**, 11448–11459.
57 A. F. M. EL-Mahdy, M. Y. Lai and S. W. Kuo, *J. Mater. Chem. C*, 2020, **8**, 9520–9528.
58 Y. F. Xie, S. Y. Ding, J. M. Liu, W. Wang and Q. Y. Zheng, *J. Mater. Chem. C*, 2015, **3**, 10066–10069.
59 G. Chen, H. H. Lan, S. L. Cai, B. Sun, X. L. Li, Z. H. He, S. R. Zheng, J. Fan, Y. Liu and W. G. Zhang, *ACS Appl. Mater. Interfaces*, 2019, **11**, 12830–12837.
60 S. L. Cai, Z. H. He, X. L. Li, K. Zhang, S. R. Zheng, J. Fan, Y. Liu and W. G. Zhang, *Chem. Commun.*, 2019, **55**, 13454–13457.
61 Z. Li, N. Huang, K. H. Lee, Y. Feng, S. Tao, Q. Jiang, Y. Nagao, S. Irle and D. Jiang, *J. Am. Chem. Soc.*, 2018, **140**, 12374–12377.
62 M. Li, Z. Cui, S. Pang, L. Meng, D. Ma, Y. Li, Z. Shi and S. Feng, *J. Mater. Chem. C*, 2019, **7**, 11919–11925.
63 F. Z. Cui, J. J. Xie, S. Y. Jiang, S. X. Gan, D. L. Ma, R. R. Liang, G. F. Jiang and X. Zhao, *Chem. Commun.*, 2019, **55**, 4550–4553.
64 Y. H. Wang, K. J. Huang and X. Wu, *Biosens. Bioelectron.*, 2017, **97**, 305–316.
65 S. B. Wang, Z. X. Chen, F. Gao, C. Zhang, M. Z. Zou, J. J. Ye, X. Zeng and X. Z. Zhang, *Biomaterials*, 2020, **234**, 119772.
66 S. Kandambeth, K. Dey and R. Banerjee, *J. Am. Chem. Soc.*, 2019, **141**, 1807–1822.
67 X. Liu, M. Hu, M. Wang, Y. Song, N. Zhou, L. He and Z. Zhang, *Biosens. Bioelectron.*, 2019, **123**, 59–68.
68 E. Cho, J. Choi, S. Jo, D. H. Park, Y. K. Hong, D. Kim and T. S. Lee, *ChemPlusChem*, 2019, **84**, 1130–1134.
69 G. U. Reddy, H. Agarwalla, N. Taye, S. Ghorai, S. Chattopadhyay and A. Das, *Chem. Commun.*, 2014, **50**, 9899–9902.
70 Y. Chen, W. Y. Li, Y. Wang, X. D. Yang, J. Chen, Y. N. Jiang, C. Yu and Q. Lin, *J. Mater. Chem. C*, 2014, **2**, 4080–4085.
71 J. Sun, F. Yang, D. Zhao, C. Chen and X. Yang, *ACS Appl. Mater. Interfaces*, 2015, **7**, 6860–6866.
72 C. Cui, Q. Wang, C. Xin, Q. Liu, X. Deng, T. Liu, X. Xu and X. Zhang, *Microporous Mesoporous Mater.*, 2020, **299**, 110122.
73 B. Guo, X. Pan, Y. Liu, L. Nie, H. Zhao, Y. Liu, J. Jing and X. Zhang, *Sens. Actuators, B*, 2018, **256**, 632–638.
74 Q. H. You, A. W. M. Lee, W. H. Chan, X. M. Zhu and K. C. F. Leung, *Chem. Commun.*, 2014, **50**, 6207–6210.
75 J. F. Folmer-Andersen, V. M. Lynch and E. V. Anslyn, *Chem. – Eur. J.*, 2005, **11**, 5319–5326.